Supplementary Information for "Twisted light from topological chiral exceptional points in a nanolaser array"

Kaiwen Ji,[1] Melissa Hedir,[2] Ramy El-Ganainy,[3] Alejandro M. Yacomotti,[1,*] and Li Ge[4,5,†]

[1] *Laboratoire Photonique Numérique et Nanosciences, Institut d'Optique d'Aquitaine, Université Bordeaux, CNRS, Rue François Mitterrand, Talence, 33400, France*
[2] *Centre de Nanosciences et de Nanotechnologies, CNRS, Université Paris-Saclay, 10 Boulevard Thomas Gobert, 91120 Palaiseau, France*
[3] *Department of Electrical and Computer Engineering, Saint Louis University, Saint Louis, MO 63103, USA*
[4] *Department of Engineering Science and Physics, College of Staten Island, CUNY, Staten Island, NY 10314, USA*
[5] *The Graduate Center, CUNY, New York, NY 10016, USA*

(Dated: July 8, 2025)

SUPPLEMENTARY NOTE 1: ABSENCE OF CHIRAL EPS IN THE "SYSTEM-WISE" APPROACH

As we mentioned in the main text, the chiral EPs in micro-ring resonators utilized the "top-down" approach that aims to achieve asymmetric scatterings between the CW and CCW traveling waves. For a compact array consisting of just four nanocavities with localized modes, a realization of this approach using a waveguide cannot be applied, whether it is an S-bend [1] or an external waveguide [2]. Similarly, placing external scatterers [3, 4] most likely has a stronger effect of spoiling the quality factor of the localized modes instead of providing a preferred tunneling direction between them.

The remaining option within the "top-down" approach features a non-uniform refractive index along a ring structure, such as a complex grating that satisfies PT symmetry [5, 6]. For example, if the real part of this grating is given by a sine function along the ring, the imaginary part can then be chosen as a cosine function. Still, this strategy is unlikely to yield a chiral EP either in our nanolaser array either, as we exemplify below.

We start with a uniform coupling $t > 0$ in our tight-binding model, and we impose a complex grating using the on-site potential modulation

$$V = at[1, 0, -1, 0]^T + ibt[0, 1, 0, -1]^T \quad (a, b \in \mathbb{R}) \tag{S1}$$

that mimics the continuous case $V(\theta) = at\cos(m\theta) + ibt\sin(m\theta)$ (where $\theta = [0, 2\pi]$ is the azimuthal angle and $m = 1$ is the angular momentum) [5]. An EP can then be found at

$$a = 0, \quad b = \pm 2 \tag{S2}$$

as Figs. S1(a,b) illustrate. These EPs can be shown to be of order 3, and the wave functions at these EPs are given by

$$\psi_{\mathrm{EP3}} = [1, \pm i, 1, \mp i], \tag{S3}$$

which are mirror *symmetric* about the line connecting sites 2 and 4, due to the same symmetry of the Hamiltonian when $a = 0$. Therefore, ψ_{EP} is *non-chiral*, which can also be shown using Eq. (S18). The other eigenstate of the Hamiltonian here can be chosen as $\psi_1 = [1, 0, -1, 0]$, and it can also be shown to have vanished OAM $\langle L_z \rangle$ using Eq. (S18).

Similarly, if we impose a step-like grating

$$V = at[1, -1, -1, 1]^T + ibt[1, 1, -1, -1]^T \tag{S4}$$

that mimics the continuous case $V(\theta) = at\,\mathrm{sgn}[\cos(m\theta)] + ibt\,\mathrm{sgn}[\sin(m\theta)]$ [6], we observe four EP lines given by

$$b = \pm 1, \quad E = \pm\sqrt{a^2 + 1} \equiv E_{\pm} \tag{S5}$$

as Figs. S1(c,d) show. Their wave functions are given by

$$\psi_{\pm} = [a + E_{\pm}, 1, -i, -i(a + E_{\pm})]^T, \tag{S6}$$

and since $a + E_{\pm}$ is real, they cannot take the form of the normalized chiral states $[1, \pm i, -1, \mp i]/2$ either with OAM $\langle L_z \rangle = \pm 1$.

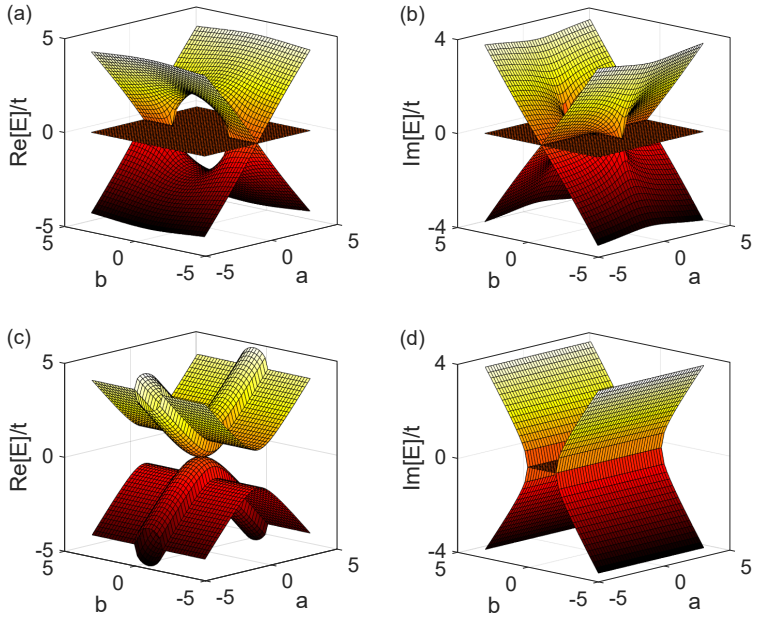

FIG. S1. (a,b) Riemann sheets for the real and imaginary parts of the complex spectrum complex with the potential given by Eq. (S1). (c,d) Same as (a,b) but for the potential given by Eq. (S4).

One reason that the two examples above fail is due to the limited OAM numbers that can be supported by a small discretized ring with 4 sites: They are either 0 or ± 1. If we want the scattering between the ± 1 OAM states to be asymmetric, then we require a $l = 2$ complex grating, which is not supported by a ring with 4 sites: We can let the real part of the grating be proportional to $[1, -1, 1, -1]$ that mimics $\cos 2\theta$ with $\theta = 0, \pi/2, \pi, 3\pi/2$, but the corresponding imaginary part is then given by $\sin 2\theta$, which vanishes at these discrete values of θ. This grating then becomes real and cannot lead to a chiral EP. Similarly, if we let the imaginary part of the grating to be proportional to $[1, -1, 1, -1]$, then the real part of the grating vanishes. This latter case corresponds to the non-Hermitian Rice-Mele model we used in the main text with $t_1 = t_2$, which does not yield a chiral EP either, because the model is mirror symmetric.

Therefore, our explorations above suggest that *only* by including the modulation of couplings can chiral EPs (i.e., with chirality ± 1) be realized in the extremely discretized systems, such as in our nanolaser array made up of four cavities. This is a completely different strategy from the continuous case, and the most effective approach is the "element-wise" approach presented in the main text using the guiding principle of consecutive $\pi/2$ jump along the array.

SUPPLEMENTARY NOTE 2: OPTICAL FLUX AND OAM

In this section, we give the expression for the optical flux [7, 8] used in the main text to introduce the guiding principle of forming a chiral mode in our nanolaser array. Within the framework of the tight-binding model (or equivalently, the coupled mode theory), the Schrödinger-like equation for the complex field amplitude at site n is given by:

$$i\frac{d\psi_n}{dt} = \omega_n\psi_n - \sum_m t_{nm}\psi_m \tag{S7}$$

Here we focus on Hermitian couplings $t_{nm} = t_{nm}^*$, and with an open boundary condition, all t_{nm}'s can be made positive after a gauge transformation. We use the same convention for our array arranged along a ring, although it has a periodic boundary condition. ω_n is the complex resonant frequency at site n, with its imaginary part representing gain or loss depending on its sign.

It is then straightforward to derive an expression for the time derivative of the optical intensity or probability amplitude $I_n \equiv |\psi_n|^2$:

$$\frac{dI_n}{dt} = -2\mathrm{Im}[\omega_n]I_n + i\sum_m t_{nm}(\psi_n^*\psi_m - c.c.) \tag{S8}$$

The first term on the right-hand side quantifies power loss or gain. Each term in the summation can be interpreted as the optical flux from site m to site n and we denote it by

$$J_{nm} = it_{nm}(\psi_n^*\psi_m - c.c.) \tag{S9}$$

which may be positive or negative. More specifically, we note $J_{n+1,n} = -J_{n,n+1}$ is the flux from site n to $n+1$, and it can expressed as

$$J_{n+1,n} = it_{n+1,n}(\psi_{n+1}^*\psi_n - c.c.) = 2t_{n,n+1}|\psi_{n+1}\psi_n|\sin(\theta_{n+1} - \theta_n), \tag{S10}$$

where $\theta_n = \mathrm{Arg}\,\psi_n$. This is the expression for the optical flux we used in the main text. We note that the flux is a physical quantity and does not change after a gauge transformation.

To show that the optical flux is directly related to OAM, we first note for an eigenstate of the Hamiltonian with a positive OAM $l > 0$, its time-dependent wave function is proportional to $e^{-iE_\mu t + il\theta}$, i.e., with a phase velocity in the CCW direction. At the same time, the increasing phase of the time-independent wave function (i.e., $e^{il\theta}$) in the CCW direction also indicates a flux $J_{n,n+1}$ in the same direction, independent of whether we label the sites in the CW or CCW direction. The sign of $J_{n+1,n}$ though does dependent on this choice, and it is positive in a CCW mode using our notation in Fig. 1a of the main text.

To make the connection between the optical flux and OAM more explicit, we derive the expression for the latter in our array. We start with the OAM defined for a vector optical field $\boldsymbol{E}$ confined to the x-y plane [9]:

$$\langle L_z\rangle = \frac{\hbar\int r dr d\phi \sum_{j=x,y,z} E_j^* \frac{\partial}{\partial\phi}E_j}{i\int r dr d\phi\, \boldsymbol{E}^*\cdot\boldsymbol{E}}. \tag{S11}$$

For a scalar wave function ψ along a ring centered at the origin, we simplify this expression to

$$\langle L_z\rangle = \frac{\hbar\int d\phi\, \psi^*\frac{d}{d\phi}\psi}{i\int d\phi\,|\psi|^2}. \tag{S12}$$

Note that now $\langle L_z\rangle$ is *dimensionless*, i.e., it gives the OAM number. For example, it is easy to check that this expression gives $\langle L_z\rangle = l$, as expected, for the OAM wave proportional to $e^{il\theta}$ considered above. Before we discretize it on a tight-binding ring, we first enforce the realness of this expression by summing it up with its complex conjugate and dividing the result by a factor of 2:

$$\langle L_z\rangle = \frac{\hbar\int d\phi\,(\psi^*\frac{d}{d\phi}\psi - c.c.)}{2i\int d\phi\,|\psi|^2}. \tag{S13}$$

For a tight-binding ring of N sites, we then use $\Delta\phi = 2\pi/N$, $\int d\phi \to \sum_{n=1}^{N} \Delta\phi$, $d\psi/d\phi \to (\psi_{n+1} - \psi_n)/\Delta\phi$, and the normalization $\sum_{n=1}^{N} |\psi_n|^2 = 1$ to derive

$$\langle L_z \rangle = \frac{\sum_{n=1}^{N} (\psi_n^* \psi_{n+1} - c.c.)}{2i} = \sum_{n=1}^{N} |\psi_{n+1}\psi_n| \sin(\theta_{n+1} - \theta_n) = \frac{1}{2} \sum_{n=1}^{N} \frac{J_{n+1,n}}{t_{n+1,n}}, \tag{S14}$$

where the index $N+1$ is equivalent to 1 due to the periodic boundary condition. It is not surprisingly that the flux in the summation needs to be divided by a quantity with the dimension of the coupling, which is needed to ensure that the OAM number is dimensionless.

For our nanolaser array with four coupled cavities, it is then clear

$$|\psi_\pm\rangle = \frac{[1, \pm i, -1, \mp i]^T}{2} \tag{S15}$$

has $\langle L_z \rangle = \pm 1$. To calculate OAM in an arbitrary state $|\psi\rangle$ on this ring, we can either apply Eq. (S14) directly, or we can use the following expansion

$$|\psi\rangle \equiv c_+|\psi_+\rangle + c_-|\psi_-\rangle + c_A|\psi_A\rangle + c_B|\psi_B\rangle, \tag{S16}$$

where

$$|\psi_A\rangle = \frac{[1, 0, 1, 0]^T}{\sqrt{2}}, \quad |\psi_B\rangle = \frac{[0, 1, 0, 1]^T}{\sqrt{2}} \tag{S17}$$

form an orthogonal basis with $\psi_\pm$. It is easy to check that $\langle L_z \rangle = 0$ in $|\psi_A\rangle$ and $|\psi_B\rangle$ due to their alternate zeros. Therefore, the OAM in $|\psi\rangle$ is given by

$$\langle L_z \rangle = |c_+|^2 - |c_-|^2 = |\langle \psi_+|\psi\rangle|^2 - |\langle \psi_-|\psi\rangle|^2. \tag{S18}$$

In the main text, we mentioned that the two modes given by Eq. (6) with $q = \pi$ have (unnormalized) wave functions

$$|\psi_\pm(\pi)\rangle = [1,\, e^{i\xi_\pm}, -1,\, -e^{i\xi_\pm}]^T \tag{S19}$$

and OAM

$$\langle L_z \rangle_\pm = \frac{2\sin(\mathrm{Re}\,\xi_\pm)}{e^{\mathrm{Im}\,\xi_\pm} + e^{-\mathrm{Im}\,\xi_\pm}} = \frac{\sin(\mathrm{Re}\,\xi_\pm)}{\cosh(\mathrm{Im}\,\xi_\pm)}. \tag{S20}$$

This result is derived using the expansion

$$|\psi_\pm(\pi)\rangle = (1 - ie^{i\xi_\pm})|\psi_+\rangle + (1 + ie^{i\xi_\pm})|\psi_-\rangle, \tag{S21}$$

which leads to

$$\langle L_z \rangle_\pm = \frac{|1 - ie^{i\xi_\pm}|^2 - |1 + ie^{i\xi_\pm}|^2}{|1 - ie^{i\xi_\pm}|^2 + |1 + ie^{i\xi_\pm}|^2} = \frac{2\mathrm{Im}[e^{i\xi_\pm}]}{1 + |e^{i\xi_\pm}|^2} = \frac{2\sin(\mathrm{Re}\,\xi_\pm)e^{-\mathrm{Im}\,\xi_\pm}}{1 + e^{-2\mathrm{Im}\,\xi_\pm}} \tag{S22}$$

from which Eq. (S20) is derived.

Now, by noticing

$$e^{i\xi_+}e^{i\xi_-} = \frac{\Delta - E_+(\pi)}{t_1 - t_2}\frac{\Delta - E_-(\pi)}{t_1 - t_2} = \frac{[\Delta - E_+(\pi)][\Delta + E_+(\pi)]}{(t_1 - t_2)^2} = -1, \tag{S23}$$

we find $\xi_+ + \xi_- = \pi$, or equivalently,

$$\mathrm{Re}\,\xi_+ + \mathrm{Re}\,\xi_- = \pi, \quad \mathrm{Im}\,\xi_+ = -\mathrm{Im}\,\xi_-. \tag{S24}$$

In other words, we have

$$\sin(\mathrm{Re}\,\xi_+) = \sin(\mathrm{Re}\,\xi_-), \quad e^{\mathrm{Im}\,\xi_+} + e^{-\mathrm{Im}\,\xi_+} = e^{\mathrm{Im}\,\xi_-} + e^{-\mathrm{Im}\,\xi_-}, \tag{S25}$$

and inserting them into Eq. (S20) gives

$$\langle L_z\rangle_+ = \langle L_z\rangle_-. \tag{S26}$$

In Supplementary Note 3, we show that this is a general property for two modes connected by the non-Hermitian chiral symmetry of our nanolaser array.

In the main text, we also mentioned that the two modes given by Eq. (6) with $q = 0$ are non-chiral, which we prove below. The wave functions of these two modes must have the form

$$|\psi_{\rm nc}\rangle = [\psi_1, \psi_2, \psi_1, \psi_2]^T \tag{S27}$$

as a result of $q = 0$. It is easy to verify that the expansion of $|\psi_{\rm nc}\rangle$ in the basis $\{|\psi_\pm\rangle, |\psi_A\rangle, |\psi_A\rangle\}$ is

$$|\psi_{\rm nc}\rangle = \sqrt{2}(\psi_1|\psi_A\rangle + \psi_2|\psi_B\rangle), \tag{S28}$$

i.e., it does not overlap with $|\psi_\pm\rangle$. Therefore, the OAM $\langle L_z\rangle$ must be zero in $|\psi_{\rm nc}\rangle$ using Eq. (S18).

SUPPLEMENTARY NOTE 3: CHIRAL SYMMETRY AND OAM

To study chiral symmetry and its zero mode in non-Hermitian photonics systematically, one convenient approach is to construct such a system utilizing the Clifford algebra [10]. For our nanolaser array with four cavities, the Hamiltonian rewritten in the sublattice basis is given by

$$H = \begin{pmatrix} \Delta & 0 & -t_1 & -t_2 \\ 0 & \Delta & -t_2 & -t_1 \\ -t_1 & -t_2 & -\Delta & 0 \\ -t_2 & -t_1 & 0 & -\Delta \end{pmatrix} \quad (t_1, t_2 > 0,\, \Delta \in \mathbb{C}). \tag{S29}$$

Since it has a 4-dimension Hilbert space, it can be analyzed using the Dirac matrices

$$\gamma^0 = \begin{pmatrix} \mathbf{1}_2 & 0 \\ 0 & -\mathbf{1}_2 \end{pmatrix}, \quad \gamma^j = \begin{pmatrix} 0 & \sigma_j \\ -\sigma_j & 0 \end{pmatrix} \ (j = 1, 2, 3), \quad \gamma^5 = \begin{pmatrix} 0 & \mathbf{1}_2 \\ \mathbf{1}_2 & 0 \end{pmatrix}. \tag{S30}$$

Here $\mathbf{1}_2$ is the 2×2 identity matrix, σ_i's are the Pauli matrices, and the sublattice operator C mentioned in the main text takes the form of γ^0. The latter gives the sublattice/chiral operator when $\Delta = 0$ (i.e., the Hermitian case). When $\Delta \neq 0$, we can write H using the Dirac matrices as

$$H = \Delta\gamma^0 + \gamma^5 - t_2\gamma^0\gamma^1. \tag{S31}$$

Using the anti-commutative properties of the γ matrices, we then identify $C_1 \equiv \gamma^1$ and $C_2 \equiv \gamma^0\gamma^5$ as two chiral operators in our system:

$$\{H, \gamma^1\} = 0, \quad \{H, \gamma^0\gamma^5\} = 0. \tag{S32}$$

We also note that our ring model has a π-rotation symmetry, and it takes the following form in the sublattice basis:

$$R = \begin{pmatrix} \sigma_x & 0 \\ 0 & \sigma_x \end{pmatrix} = R^{-1}. \tag{S33}$$

It is easy to verify that $[H, R] = 0$. In general, if $[H, X] = 0$, then XC_iX^{-1} $(i = 1, 2)$ is also a chiral symmetry of our ring model. Here with $X = R$ though, this "new" chiral operator is identical to C_i. The chiral operators of our ring model warrant a symmetric spectrum of H about the origin in the complex energy plane, i.e., $E_\mu = -E_\nu$, as well as $\psi_\nu \propto C_i\psi_\mu$. An EP is formed at $E = 0$ in our ring model when $\mu = \nu$.

Next we show that a pair of modes connected by C_1 has the same OAM. For this purpose, we use Eq. (S18) to calculate $\langle L_z \rangle$. We first choose the proper sign in the normalization such that $\psi_\nu = C_1\psi_\mu$. We then transform ψ_μ, ψ_ν back to the original space basis using

$$U = \begin{pmatrix} 1 & & & \\ & 0 & 1 & \\ & 1 & 0 & \\ & & & 1 \end{pmatrix} = U^{-1}. \tag{S34}$$

In the space basis, they now satisfy

$$\psi_\nu = (U\gamma^1U^{-1})\psi_\mu \equiv \gamma_s^1\psi_\mu, \quad \gamma_s^1 = \begin{pmatrix} & & & 1 \\ & & -1 & \\ & 1 & & \\ -1 & & & \end{pmatrix} = (\gamma_s^1)^{-1}. \tag{S35}$$

Using Eq. (S18), the OAM of ψ_μ, ψ_ν is given by

$$\langle L_z \rangle_\mu = |\langle \psi_+ | \psi_\mu \rangle|^2 - |\langle \psi_- | \psi_\mu \rangle|^2, \quad \langle L_z \rangle_\nu = |\langle \psi_+ | \psi_\nu \rangle|^2 - |\langle \psi_- | \psi_\nu \rangle|^2. \tag{S36}$$

Using

$$\langle \psi_+ | \psi_\nu \rangle = \langle \psi_+ | \gamma_s^1 \psi_\mu \rangle = -i\langle \psi_+ | \psi_\nu \rangle, \quad \langle \psi_- | \psi_\nu \rangle = \langle \psi_- | \gamma_s^1 \psi_\mu \rangle = i\langle \psi_+ | \psi_\nu \rangle, \tag{S37}$$

we then find

$$\langle L_z \rangle_\mu = \langle L_z \rangle_\nu. \tag{S38}$$

SUPPLEMENTARY NOTE 4: r-DEPENDENCE AND RESILIENCE OF THE OAM

In this section, we discuss the r-dependence of the OAM and the value of r at the CEP (denoted $r_{\rm EP}$ below), once t_1, t_2, α, and $P_{\rm total}$ are known.

In the linear regime where gain/loss saturation is negligible, g_j is given by $(P_j/\gamma_{\rm tot} - n_0)\beta\gamma_\parallel/2$, where $\gamma_{\rm tot}, \gamma_\parallel, n_0, \beta$, are the total carrier recombination rate, the two-level radiative combination rate, the carrier number at transparency, and spontaneous emission coefficient, respectively. Therefore, we find

$$g_A - g_B = (P_A - P_B)\frac{\beta\gamma_\parallel}{2\gamma_{\rm tot}} = -r\frac{P_{\rm tot}\beta\gamma_\parallel}{2\gamma_{\rm tot}}. \tag{S39}$$

In the main text, we showed that $g_A - g_B = -2(t_1 - t_2)$ for a CW CEP. Therefore, with our choice $t_1 > t_2 > 0$, its realization requires a positive $r_{\rm EP}$:

$$r_{\rm EP} = \frac{4(t_1 - t_2)}{p}, \quad p \equiv \frac{P_{\rm tot}\beta\gamma_\parallel}{\gamma_{\rm tot}}. \tag{S40}$$

For example, with $t_1 = 10.7$, $t_2 = 9.5$, $p = 9.1$, we find $r_{\rm EP} = 0.53$ as in Fig. 2c of the main text. We also showed in the main text that $\Delta_0 = \alpha(t_1 - t_2)$ to reach a CW CEP, with which we write

$$\Delta = \alpha(t_1 - t_2) - \frac{i + \alpha}{4}rp. \tag{S41}$$

Clearly, Δ becomes imaginary and equals $-i(t_1 - t_2)$ at $r_{\rm EP} = 0.53$ in this example as expected.

With $\alpha = 3$ as in Fig. 2c of the main text, we plot the OAM $\langle L_z \rangle$ in Fig. S2 using Eq. (S20) (solid line), and it agrees qualitatively with the COMSOL simulation in Fig. 2c of the main text, with a node at $r = 0$ (where the system is effective Hermitian) and its maximum at $r_{\rm EP} = 0.53$. Note that on the negative side of $r \in [-1, 0]$, the OAM is close to 0 and hence not plotted. The CCW CEP exists in this range only if Δ_0 is negative instead.

In the same figure, we also consider the case where Δ_0 deviates slightly from the ideal value, which is more likely the case in both the COMSOL simulation and experiments. With Δ_0 off by $\pm 10\%$, we observe that $\langle L_z \rangle$ displays the same trends as in the ideal case, which is another evidence of the resilience of our system.

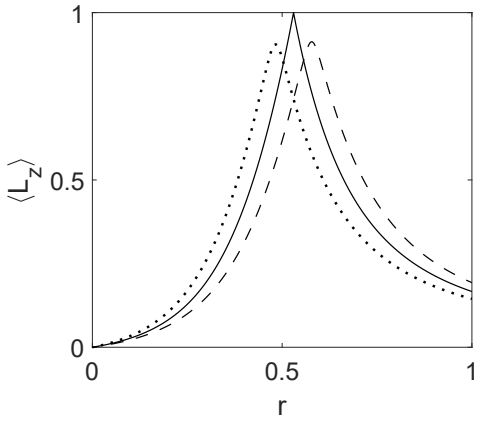

FIG. S2. Change of the OAM number as a function of the pump imbalance. Solid line show the ideal case. Dotted and dashed lines show the cases where Δ_0 is 90% and 110% of its ideal value.

SUPPLEMENTARY NOTE 5: STOCHASTIC NONLINEAR RATE EQUATIONS

The semiconductor photonic crystal nanolaser discussed in the main text belongs to the class-B laser, characterized by carrier lifetimes much longer than photon lifetimes. As a result, the carrier dynamics cannot be adiabatically eliminated. Therefore, a complete description of the system operating above the lasing threshold requires the use of coupled rate equations that explicitly incorporate both carrier populations and cavity fields:

$$\frac{da_j}{dt} = H_{\mathrm{NL}} a_j + F_j(t) \tag{S42}$$

$$\frac{dn_j}{dt} = P_j - \gamma_{\mathrm{tot}} n_j - \beta\gamma_{\parallel}(n_j - n_0)|a_j|^2 \tag{S43}$$

here, a_j and n_j are the complex fields and carrier numbers in jth cavities. $H_{\mathrm{NL}} = H + \alpha g_j \mathbf{I}_4$, with $g_j = \frac{1}{2}(n_j - n_0)\beta\gamma_{\parallel}$. $F_j(t)$ represents the Langevin noise, which accounts for spontaneous emission and is characterized as white noise: $\langle F_\mu(t) F_\nu(t')\rangle = 2D_{\mu\nu}\delta(t-t')$. The coefficient is $2D_{a_i a_i^*} = 2D_{a_i a_i^*} = R_{\mathrm{SP}}$, with R_{SP} being the spontaneous emission rate $R_{\mathrm{SP}} = \beta F_p B n_j^2 / V_a$. The definitions of other physical parameters and their corresponding values are summarized in the table below.

TABLE I. List of the variables and parameters used in the stochastic equations

Symbol	Physical quantity	Values
κ	Photon loss rate	140 GHz
n_0	Carrier number at transparency	16000
α	Linewidth enhancement factor	3
β	Spontaneous emission coefficient	0.017
$\gamma_{\parallel}$	Two-level radiative recombination rate	2.2 GHz
γ_{tot}	Total carrier recombination rate	5 GHz
V_a	Volume of the active medium	0.016×10^{-12} cm^3
B	Bimolecular radiative recombination rate	3×10^{10} cm^3 s^{-1}
F_P	Purcell factor	1.03

These equations can be numerically integrated using the Euler–Maruyama method. The optical spectra are then obtained by performing a Fourier transform of the resulting time traces. Figure S3 illustrates several intriguing dynamical behaviors of the system. Notably, mode-beating limit-cycle oscillations emerge under uniform pumping conditions (lower panel of Fig. S3). Furthermore, numerical simulations reveal Q-switch self-pulsing [11] when the system operates close to the CEP, as depicted in the upper panel.

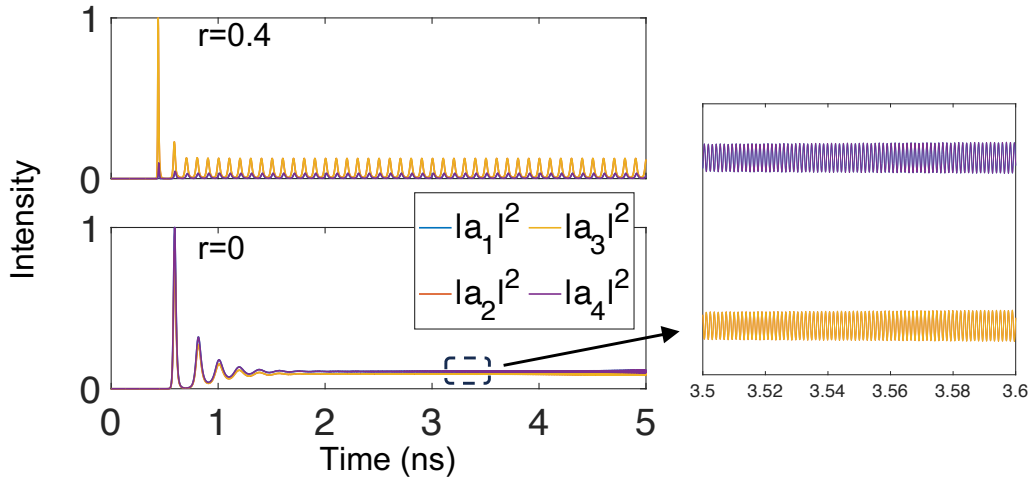

FIG. S3. Time traces at different values of r showing self-pulsing (top panel) and mode-beating (lower panel).

SUPPLEMENTARY NOTE 6: OFF-DIAGONAL FOURIER FILTERING

In order to increase the contrast of the interference pattern, we applied off-diagonal Fourier filtering technique. We assume the complex fields in the two arms of the Sagnac interferometer, denoted as A_s and A_r, can be expressed as:

$$A_s = a_s(r)e^{-i(\omega t - t_s r + \phi)}, \tag{S44}$$

$$A_r = a_r(r)e^{-i(\omega t - t_r r)}. \tag{S45}$$

Therefore, the intensity distribution of the interference patterns is given by:

$$I = |A_s + A_r|^2 = |a_s|^2 + |a_r|^2 + \left(a_s a_r^* e^{-i(\Delta k r + \phi)} + c.c\right), \tag{S46}$$

where Δk is the in-plane wavevector difference and $c.c$, denotes the complex conjugate.

Performing a two-dimensional Fourier transform on this intensity pattern, the first two terms—corresponding to the non-interfering background—produce a central peak in reciprocal space. The remaining interference terms manifest as two satellite peaks symmetrically displaced by $\pm\Delta k$, as illustrated in Fig. S4(b). Therefore, we further implement a bandpass filter, as shown in Fig. S4(c), which selectively retains only these satellite peaks. Finally, an inverse Fourier transform of the filtered reciprocal-space image yields the enhanced-contrast interference pattern, as demonstrated in Fig. S4(d).

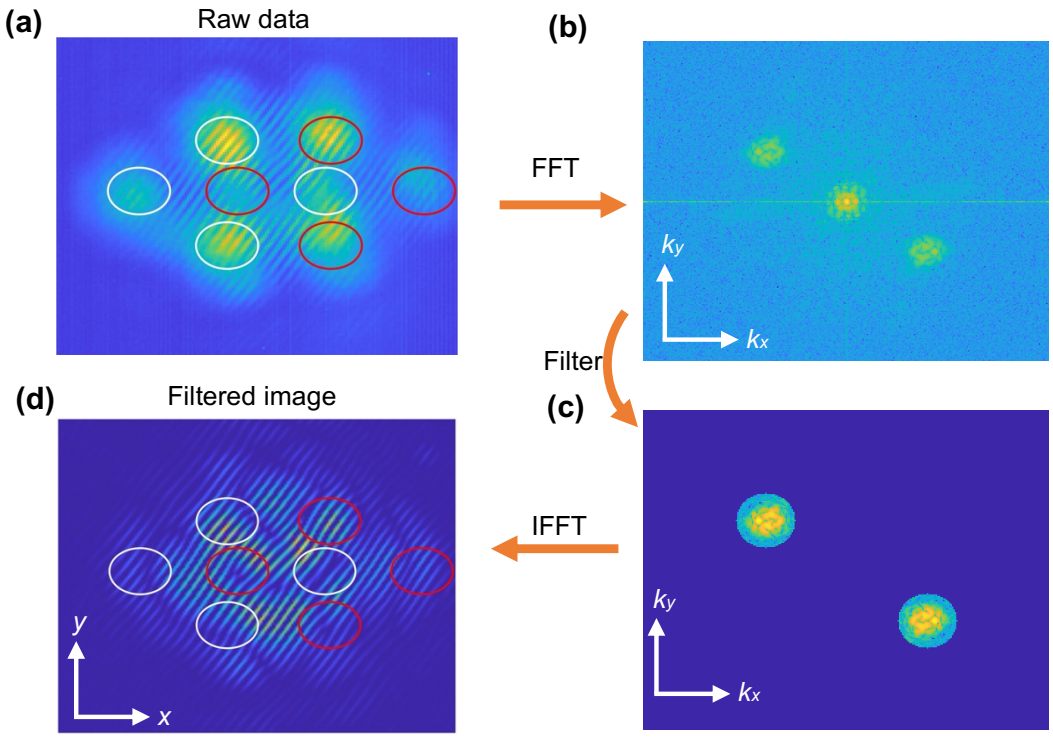

FIG. S4. Off-diagonal Fourier filter technique

Moreover, this method enables extraction of the spatial phase information from the interference patterns. We first apply a bandpass filter to isolate one of the satellite peaks, which carries the complex phase information described by $\mathbf{F}[a_s a_r^* e^{-i(\Delta k r + \phi)}]$. This selected satellite is subsequently re-centered by performing a rigid translation of $-\Delta k$, as shown in Fig. S5(b). Consequently, the resultant peak in reciprocal space corresponds to $\mathbf{F}[a_s a_r^* e^{-i\phi}]$. The spatial distribution of the phase can thus be recovered by executing an inverse Fourier transform on this filtered satellite and calculating its argument, as demonstrated in Fig. S5(c).

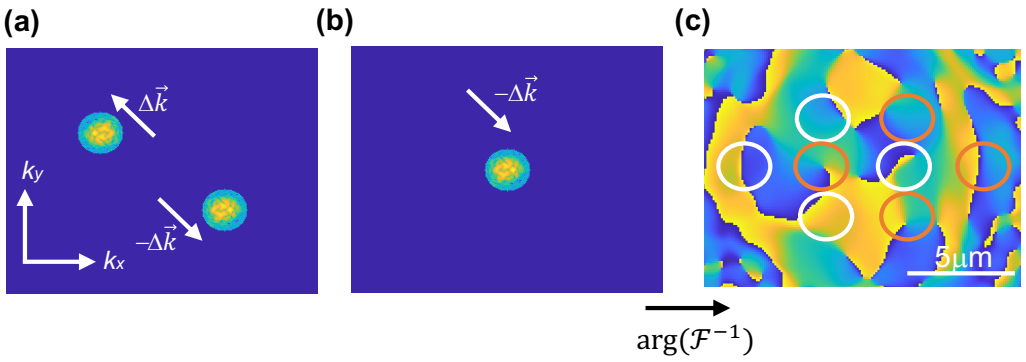

FIG. S5. Spatial phase retrieving technique.

SUPPLEMENTARY NOTE 7: SAMPLE DESIGN AND FINITE ELEMENT SIMULATIONS

The structure we simulated is illustrated in Fig. S6 a. The lattice constant $a = 414$nm. The orange-colored holes are introduced to fold the band structure and enhance the emission beaming efficiency. The blue holes are reduced in size and displaced by a distance $d = 0.16a$ to increase the quality (Q) factor. The coupling difference is achieved by altering the size of the red holes. The resonance wavelengths of the four modes are numerically simulated as functions of the barrier perturbation parameter h. The results are displayed in Fig. S6 b.

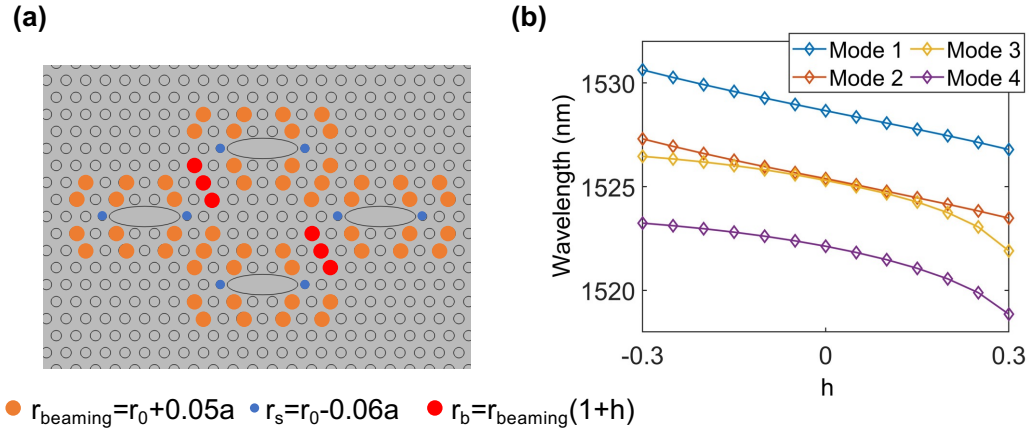

FIG. S6. (a) Detailed schematic of the simulated structure. (b) Wavelengths of the modes as a function of the barrier size. In the simulations we set $a = 414$nm, $r = 0.266a$, $n = 3.3$ and the thickness of the PC slab is $d = 265$nm.

SUPPLEMENTARY NOTE 8: EXPERIMENTAL DETAILS

The complete experimental configuration is illustrated in Fig. S7. A pulsed laser (100 ps duration and 10 Mhz repetition rate) at 800 nm is employed to minimize thermal effects. The overall pump power is controlled by an acousto-optic modulator (AOM). To shape the spatial profile of the pump beam, we employ a spatial light modulator (SLM) operating in amplitude mode. A first half-wave plate placed immediately after the AOM maximizes power transmission through the polarization beam splitter (PBS), while a second half-wave plate located just before the SLM is rotated by 22.5° to remove the background and enhance pattern contrast. The modulated pump beam is focused onto the sample using a microscope objective (100x magnification and numerical aperture 0.95). The radiation from the sample is collected by the same objective and spectrally resolved by a spectrometer.

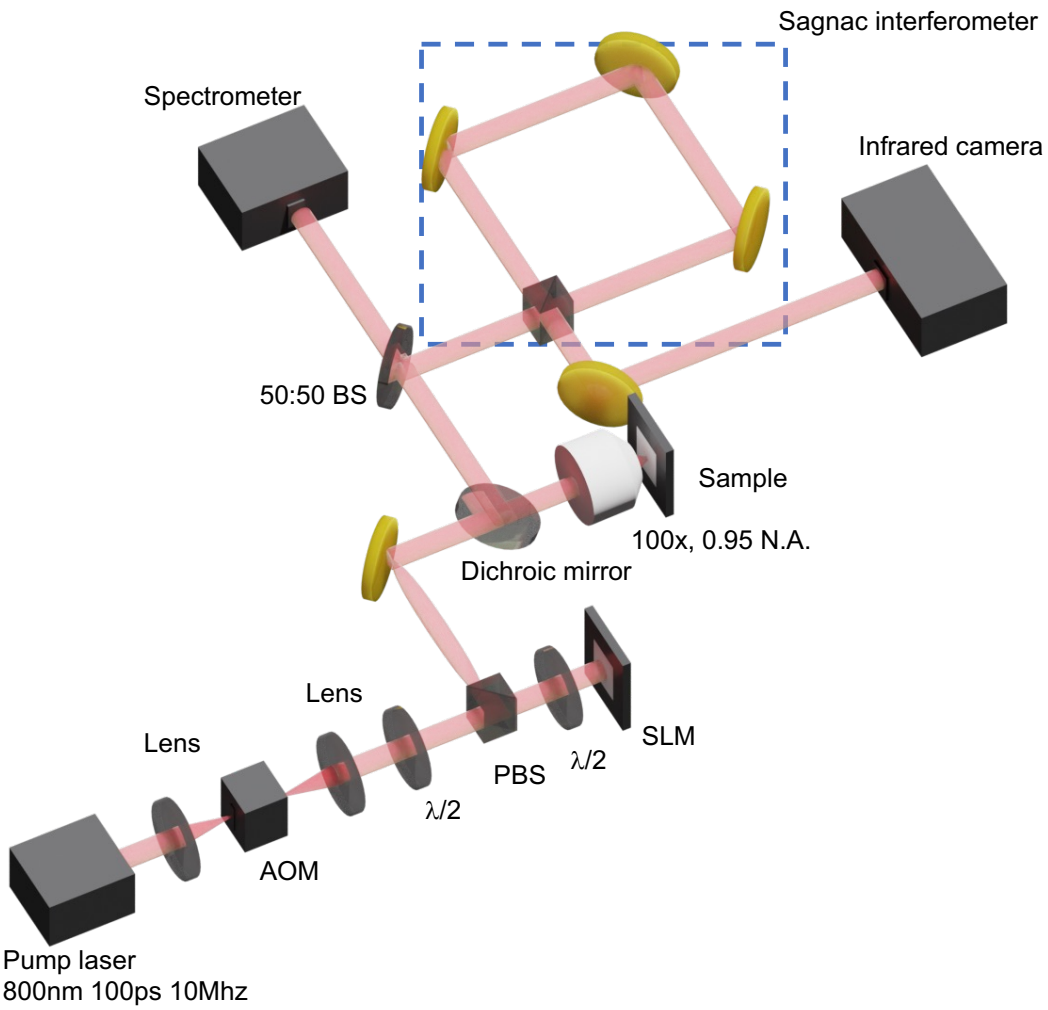

FIG. S7. Experimental setup.

* alejandro.giacomotti@institutoptique.fr
† li.ge@csi.cuny.edu

[1] W. E. Hayenga, M. Parto, J. Ren, F. O. Wu, M. P. Hokmabadi, C. Wolff, R. El-Ganainy, N. A. Mortensen, D. N. Christodoulides, and M. Khajavikhan, ACS Photonics **6**, 1895 (2019).
[2] Q. Zhong, J. Ren, M. Khajavikhan, D. N. Christodoulides, S. K. Ozdemir, and R. El-Ganainy, Phys. Rev. Lett. **122**, 153902 (2019).
[3] B. Peng, Ş. K. Özdemir, M. Liertzer, W. Chen, J. Kramer, H. Yılmaz, J. Wiersig, S. Rotter, and L. Yang, Proceedings of the National Academy of Sciences **113**, 6845 (2016).
[4] J. Wiersig, Phys. Rev. Lett. **112**, 203901 (2014).
[5] L. Feng, Z. J. Wong, R.-M. Ma, Y. Wang, and X. Zhang, Science **346**, 972 (2014).
[6] H.-Z. Chen, T. Liu, H.-Y. Luan, R.-J. Liu, X.-Y. Wang, X.-F. Zhu, Y.-B. Li, Z.-M. Gu, S.-J. Liang, H. Gao, et al., Nat. Phys. **16**, 571 (2020).
[7] L. Ge, K. G. Makris, and L. Zhang, Phys. Rev. A **96**, 023820 (2017).
[8] L. Ge, Z. Gao, and L. Feng, Phys. Rev. B **108**, 104111 (2023).
[9] Z. Shao, J. Zhu, Y. Chen, Y. Zhang, and S. Yu, Nat. Commun. **9**, 1 (2018).
[10] J. D. Rivero and L. Ge, Physical Review B **103**, 014111 (2021).
[11] A. Yacomotti, S. Haddadi, and S. Barbay, Physical Review A—Atomic, Molecular, and Optical Physics **87**, 041804 (2013).